Friction https://mc03.manuscriptcentral.com/friction
https://doi.org/10.26599/FRICT.2025.9441211

Research Article

Rail damage patterns and contact state evolution characteristics of electromagnetic launch

Luyao Liu[1], Hongshun Liu[1,*], Pengfei Lu[1], Jingtong Feng[1], Haoxi Cong[2], Li Zhang[1]

[1] *Shandong Provincial Key Laboratory of Advanced Power Transmission Technology and Intelligent Equipment, School of Electrical Engineering, Shandong University, Jinan 250061, China*

[2] *State Key Laboratory of Alternate Electrical Power System with Renewable Energy Sources, North China Electric Power University, Beijing 102206, China*

* Corresponding author: Hongshun LIU, E-mail: lhs@sdu.edu.cn

Received: August 20, 2025; Revised: November 5, 2025; Accepted: December 26, 2025

Abstract: The rail damage characteristics are a crucial factor affecting the contact quality in electromagnetic launch, while the interface current and temperature are critical parameters determining the contact state. To improve launch quality and guide equipment design, this paper establishes an electromagnetic launch experimental and testing platform to analyze the rail surface damage patterns. Based on the experimental results, simulation models for different contact states are constructed, and the interface electrothermal characteristic distribution is calculated. The results indicate that mechanical friction occurs initially between the armature and rail, followed by the formation of a liquid metal film under the action of high-temperature, which not only reduces surface roughness but may also trigger gap discharge. Increased peak value of the pulse current and the number of launches exacerbate the damage. During the launch process, current density and high-temperature areas are primarily concentrated at the rear end of the armature-rail contact surface and in regions with high curvature, with abrupt changes observed at phase transition points. Finally, considering the variation of contact resistance, optimization proposals are presented for the front, middle, and rear segments of the rail.

Keywords: contact status; electrothermal characteristics; electromagnetic launch; rail damage

1 Introduction

Electromagnetic railgun technology has been widely applied in both military and civilian fields in recent years due to its advantages of high speed, energy efficiency, and excellent controllability [1]. However, operating under extreme conditions involving high current, high temperature, and high speed [2], friction and ablation damage will occur between the rail and armature, severely affecting the contact state [3]. Reliable contact is essential for ensuring launch quality [4]. Clarifying the rail damage patterns and revealing the contact state evolution characteristics is of great significance for extending equipment lifespan and optimizing component design.

The extreme conditions and complex structure of electromagnetic launching limit experimental measurement methods. To investigate the damage characteristics of the armature and rail, an inner bore damage detection system was used to capture the damage morphology [5] [6]. After disassembling the device, measurements were conducted on the armature wear rate [7] [8] and deposition layer thickness [9]. However, existing studies are mostly focused on armature wear or qualitative observations, with limited quantitative analysis of track damage. To compensate for the experimental limitations, models such as the launcher internal ballistic [10], static wear [3] [11] and thermal melting [12] were developed to calculate the wear volume of armature and rail, as well as the heat and forces during the launch process. However, changes in the actual contact surface roughness were not considered during modeling. After launching, the rail becomes rough due to wear, corrosion, or adhesion of deposit layers [13] [14]. Surface roughness and contact resistance are important indicators of electrical contact performance [15] and are affected by current intensity and the number of launches [16]. Due to the passage of high currents or the accumulation of repeated friction, significant thermal energy is generated during electromagnetic launching [17]. Under the influence of temperature rise, the armature with a lower melting point, melts first [18], forming a liquid metal film (LMF) [19]. On one hand, the LMF may adhere to the rail, altering the contact interface roughness. On the other hand, the presence of LMF changes the armature-rail contact state, affecting contact resistance and heat generation [20]. To assess the contact condition of the armature-rail system, contact resistance was obtained using methods such as static measurement [21], empirical formulas [22], [23], and model inversion [24], [25]. Changes in the electrical contact performance of armature-rail were analyzed. However, previous analyses have primarily focused on isolated studies of electrical or thermodynamic factors, without fully exploring the correlation between contact resistance and armature-rail damage state.

In this work, we build an electromagnetic rail launch experimental platform and conducted experiments with varying pulse current peaks and launch times. After recovery of the launched rail samples, microscopic detection techniques are employed to measure the damage status of rails. Based on the experimental results, armature-rail models for different contact states are developed to analyze the variations in current and temperature during the launch process. Finally, combining the evolution of contact resistance, optimization proposals for the electromagnetic launch device are proposed. The key contributions of this work are as follows.

1) Due to the lack of research on quantitative assessment of rail damage, SEM and EDS

technologies are used to clarify the microscopic composition of the rail surface. LSM technology is employed to measure the surface roughness, providing a data foundation for modeling.

2) Addressing the issue of ignored roughness in current modeling, meta-wave theory and magnetohydrodynamics are introduced to construct a random rough surface, enabling simulations of different contact states of the armature-rail system.

3) In response to the isolation of current contact resistance research, the intrinsic relationship between rail damage morphology and contact resistance is thoroughly considered, revealing the evolution characteristics of the contact state.

The rest of this paper is organized as follows. Section 2 describes the experimental platform. Section 3 presents the experimental results of rail damage. Section 4 analyzes the electrical and thermal characteristics of armature-rail in different contact states. Section 5 discusses the evolution of contact resistance with respect to contact states, and proposes optimization strategies for the device. Finally, Section 6 concludes this paper.

2 Experimental Apparatus and testing methods

Based on the principle of current equivalence [26], an electromagnetic launch experimental and testing platform is constructed, with its circuit diagram and physical photograph shown in Fig. 1.

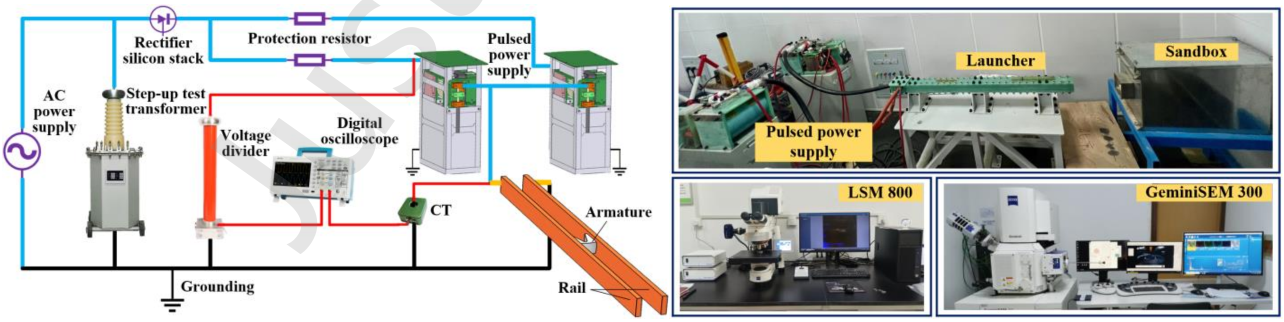

Fig. 1 Circuit diagram and physical photograph of the electromagnetic launch experimental and testing platform.

As depicted in Fig. 1, the experimental platform consists of a charging circuit, a launch circuit, and a testing system. The AC power supply is rectified by a silicon stack to charge the capacitor bank, providing pulse current excitation for the launcher. The total length of the rail in the launcher is 1.2 m, with a cross-section of 24 mm×2 mm. Its inner cavity forms a rectangular aperture of 15 mm×20 mm, and is made of C45 carbon structural steel. The armature is designed with a C-shaped solid structure, measuring 27 mm in length and 15 mm in width. It is in close contact with the rail, and is made of 6063-T6 aluminum alloy. The performance parameters of both materials are listed in Table 1 [27], [28]. The armature is positioned at an initial distance of 150 mm from the breech to ensure sufficient electromagnetic force for muzzle ejection. The rail is encapsulated externally with organic polymer and fixed in place using bolts, providing both insulation and structural support. The voltage and current of the launch circuit are connected to an oscilloscope for real-time measurement through a voltage divider and current transformer. After recovery of the rail samples following launch, a Schottky field emission scanning electron microscopy, GeminiSEM 300 equipped with an energy dispersive spectrometer (EDS) is used to obtain the micro morphology and elemental composition of the rail surface. A laser scanning microscope, LSM 800 is used to measure the surface profile and roughness of rail.

Table 1 Performance parameters of armature and rail materials

Parameters	C45 steel rail	6063-T6 aluminum alloy armature
Density (293.15 K)	7.85 g/cm^3	2.70 g/cm^3
Melting point	1768.15-1783.15 K	888.15-928.15 K
Thermal conductivity (293.15 K)	48 W/ (m·K)	198 W/(m·K)
Brinell hardness (HBW)	232-262 HB	75-90 HB
Tensile strength	≥600 MPa	≥205 MPa

3 Rail Surface Damage Patterns

To investigate the influence of pulse current peak and number of launches on rail surface damage, three sets of electromagnetic launch experiments are conducted for different conditions, as follows:

1) The pulse power supply is charged to 2000 V, producing the pulse current with a peak of 40 kA, and launch once.

2) The pulse power supply is charged to 5500 V, producing the pulse current with a peak of 130 kA, and launch once.

3) The pulse power supply is charged to 2000 V, producing the pulse current with a peak of 40 kA, and launch 10 times.

3.1 Macroscopic damage morphology

After completing each set of launch experiments, the steel rail inside the launcher is removed, and rail segment samples are selected from four typical positions along the launch direction. Each segment is 20 mm in length and is labeled as R1-1 to R1-4, R2-1 to R2-4, and R3-1 to R3-4, as shown in Fig. 2. Among these, Position I is located at the starting point of armature, 150 mm from the rail end. Position II is 375 mm from the rail end. Position III is 945 mm from the rail end, and Position IV is at the muzzle, 1200 mm from the rail end. The macroscopic damage morphology of the rail samples is compared and observed.

For Rail 1 in Fig. 2, at R1-1, the rail surface primarily exhibits transverse scratches and grooves along the launch direction, with local white deposits. At R1-2, the scratches and grooves become more numerous and denser, and the coverage of the white deposits significantly expands. At R1-3, there is a trend of reduced damage, with fewer scratches and deposits, which are more concentrated at the edges. The distribution characteristics of deposits are consistent with the research findings of Prof. Xia S G's team at Huazhong University of Science and Technology [29]. The most severe damage is found at R1-4, where, in addition to scratches and pittings, black ablation marks appear at the very front end of the rail.

Compared to Rail 1, as the pulse current increases, the scratches on the surface of Rail 2 increase and are arranged in a more compact and orderly manner. Even at Position III, where the damage is less severe at Rail 1, R2-3 still shows noticeable grooves, and the severely damaged area shifts from the edge to the central part. This is caused by the current transfer effects during the launching process [29]. As the current increases, the current density distribution will concentrate from the edges toward the center, resulting in an increase in pressure at the center. Additionally, the flow of molten aluminum liquid driven by electromagnetic force also tends to migrate inward, leaving behind more pronounced deposition patterns.

Comparing Rail 1 and Rail 3, as the number of launches increases, the damage morphology of the rail surface becomes more complex. At R3-1, in addition to transverse scratches, there are also pits of varying depths. At R3-2, the wear marks almost completely cover the entire contact surface, which is as wide as the armature. At R3-3, there are almost no regularly arranged scratches, but instead, a flaky transition ablation morphology covers the surface [30], along with typical droplet-shaped gouging pits [31]. At R3-4, white deposits intertwine with pits, grooves, and metal flow marks intertwine, forming an irregular flowing tissue.

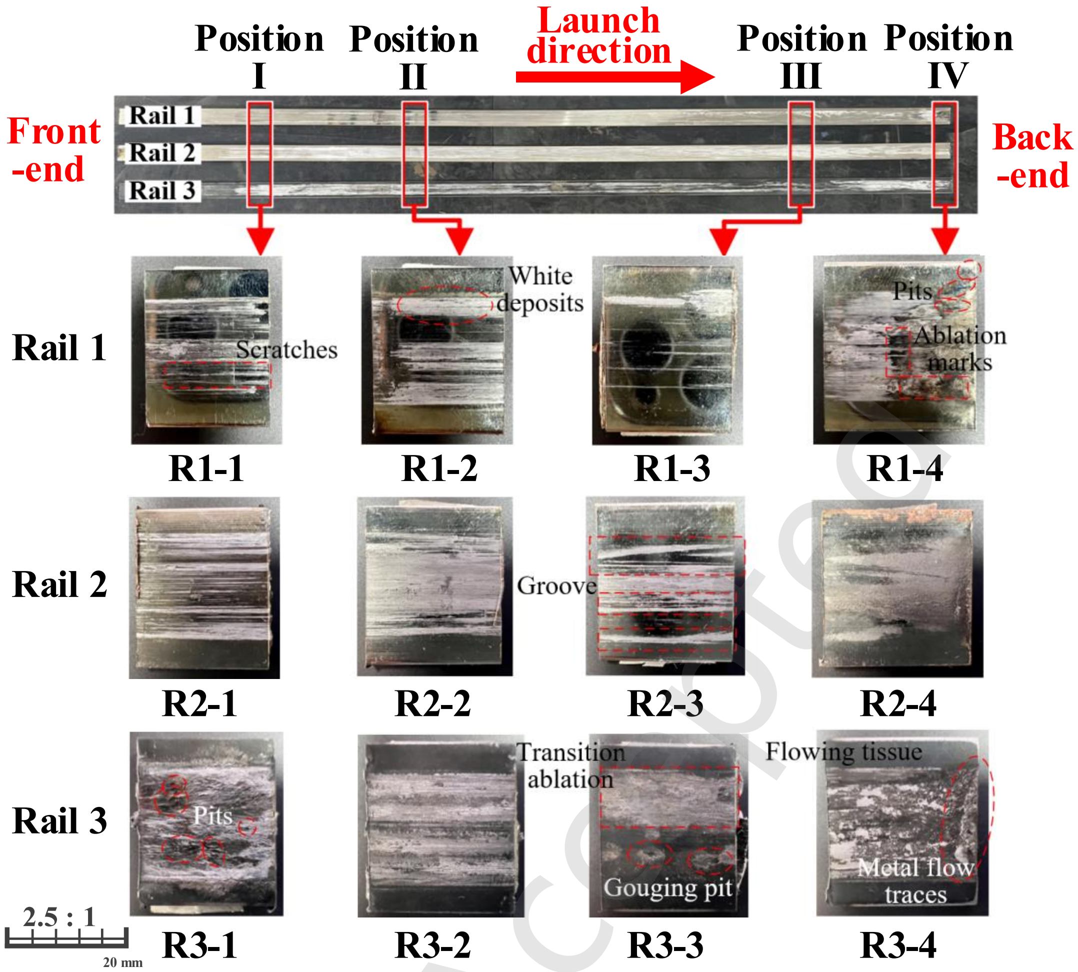

Fig. 2 Macroscopic damage morphology of different rail samples.

3.2 Microscopic composition and surface roughness

To clarify the microscopic composition of the rail surface, SEM and EDS analysis are conducted, as shown in Fig. 3.

Referring to Figs. 2 and 3, it can be seen that the white deposits on the carbon steel rail surface are the products left behind by the melting and condensation of the aluminum alloy armature, while the black marks are the result of metal oxidation and carbonization ablation. The content of Al and O elements at the rear end of rail is generally higher than that at the front end, with significantly higher levels in each segment of Rails 2 and 3 compared to Rail 1. In other words, as wear intensifies, the Al deposits and oxides on the surface increase, indicating complex solid-liquid phase transformation and material transfer between the rail and armature, ultimately forming the flowing morphology seen on R3-4 in Fig. 2 and in Fig. 3(l).

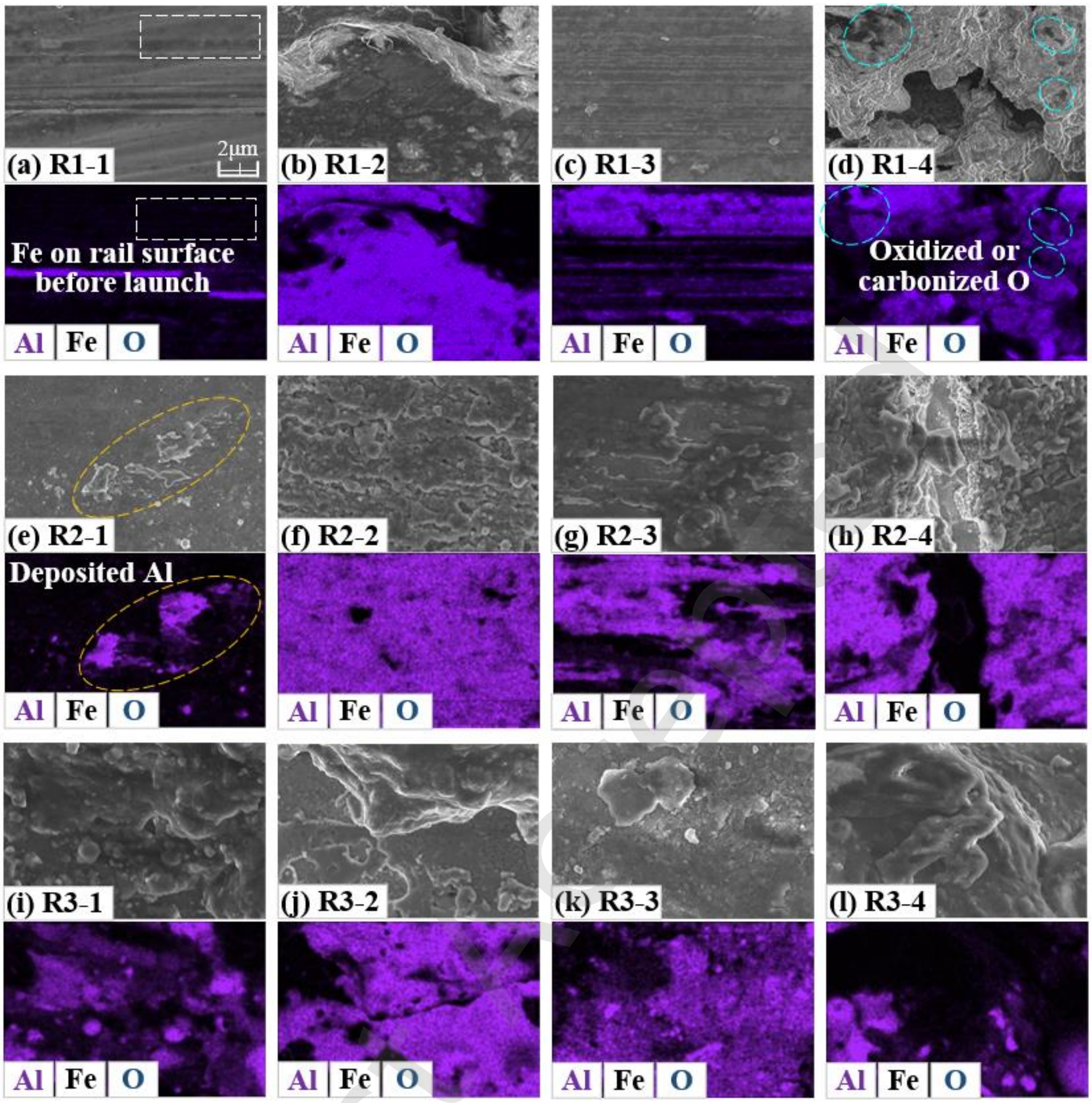

Fig. 3 Microstructure and composition of rail surface.

Furthermore, to quantitatively assess the degree of rail damage, full-area scanning of all samples is performed using LSM 800. Three-dimensional contour images are obtained at 100× magnification, and typical example of scanning results of rails before and after launch is shown in Fig. 4.

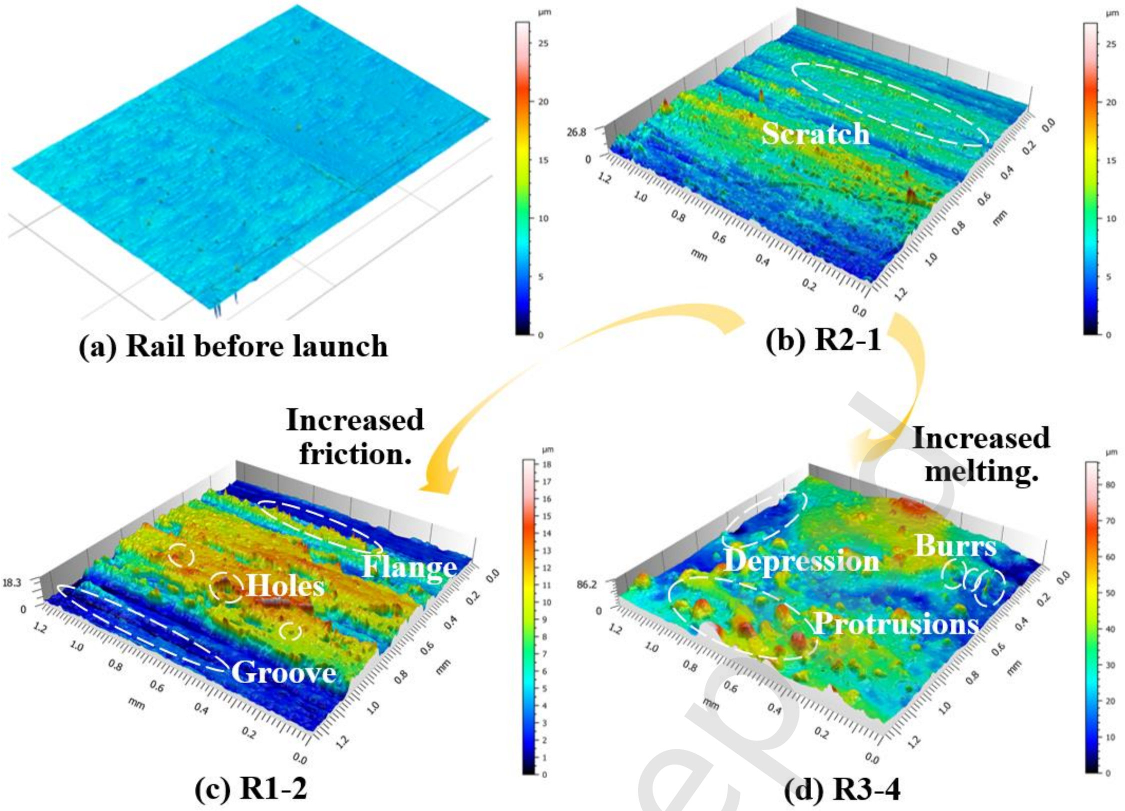

Fig. 4 Typical example of three-dimensional contour of rail damage before and after launch.

From Fig. 4(a), it is observed that the rail surface before launch is relatively smooth, with overall profile fluctuations controlled within 1.5 μm. After launching, parallel scratches are observed, as shown in Fig. 4(b). As friction intensifies, the regularly arranged raised strips transform into deeper grooves and flanges, accompanied by the formation of localized ablation holes, as shown in Fig. 4(c). With further melting, sharp burrs and even hill-like protrusions appear on the surface, while minute holes expanding into larger depressions or spalling pits, as shown in Fig. 4(d). The measured results from all samples were statistically analyzed to calculate the root mean square deviation, S_q, and explore the variation in rail damage surface roughness at different operating conditions:

$$S_q = \sqrt{\frac{1}{D}\iint_D Z^2(x, y)\,\mathrm{d}x\,\mathrm{d}y} \tag{1}$$

where, D represents the area of the measured region, and $z(x, y)$ denotes the surface height deviation at any point, (x, y), within the region. For the pre-launch rail, the average value was calculated by measuring all samples, yielding an initial S_q of 0.68 μm.

First, compare the S_q of Rail 1 and Rail 2 to analyze the impact of the pulse current peak, as shown in Fig. 5.

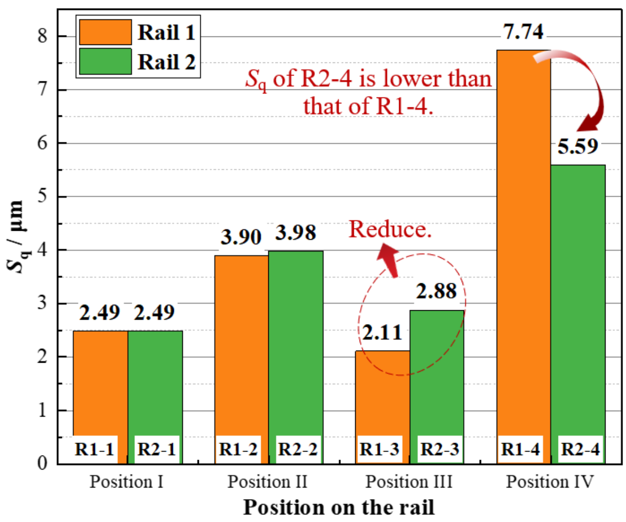

Fig. 5 Variation in S_q for Rail 1 and Rail 2.

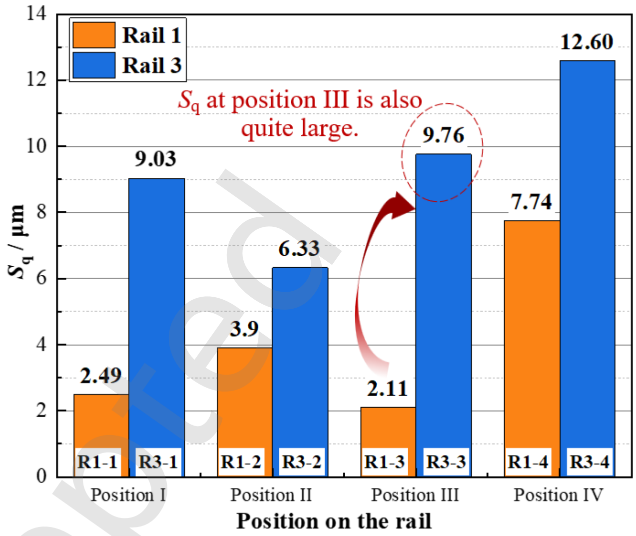

Fig. 6 Variation in S_q for Rail 1 and Rail 3.

As illustrated in Fig. 5, along the launch direction, S_q shows an overall upward trend, decreasing only at Position III. Wear at Position I is relatively mild. As the launch progresses, the current amplitude increases, leading to higher contact pressure between the rail and armature, and the intensified wear leads to an increase in S_q. Similarly, Rail 2, which carries a higher current, experiences more severe damage than Rail 1. However, when moving to Position III, due to the continuously increasing speed of the armature, the time spent in contact with the rail relatively shortens, and the duration of stress and heat also reduces, causing S_q to decrease. Until the armature exits the muzzle, the damage at Position IV is the most severe due to phenomena including high-temperature melting and metal vapor caused by muzzle arc and reflux arc [32]. However, unlike the previous three positions, S_q at R2-4 is lower than at R1-4. This is because at R1-4, the molten Al layer intertwines with the eroded steel rail, accumulating with carbonized metal particles, which causes the surface to turn black (as shown in Fig. 2). When the current increases to 130 kA, the high-speed relative displacement between the armature and rail triggers material peeling and splashing. On one hand, the deposited Al layer is continuously consumed. on the other hand, the softened molten metal fails to adhere to the rail surface in time and splashes away, or even vaporizes under the high temperature generated by arc. Therefore, the rail substrate that has been smoothed by high-speed wear is exposed, leading to a decrease in S_q of Rail 2.

Comparing the S_q of Rail 1 and Rail 3 to analyze the impact of the number of launches, as shown in Fig. 6.

As presented in Fig. 6, multiple launches not only lead to an overall increase in S_q but also change its trend. At R3-1, due to severe scraping, the surface is densely covered with scratches and pits, causing S_q to increase from 2.49 μm at R1-1 to 9.03 μm. At R3-2, regular abrasion marks are formed, and S_q decreases instead. At R3-3, flaky Al deposition layers and droplet-shaped gouging pits are formed, causing S_q to rise again. At R3-4, the fish scale-like Al deposition layer intertwines with flowing-like ablation tissues, resulting in the highest S_q value of 12.60 μm.

According to the experimental results, the initial state between the armature and rail is solid-to-solid dry sliding. Due to friction and high temperature, the aluminum alloy melts first and forms a LMF, transforming into solid-liquid-solid contact. As material is lost, gaps are created, which may also lead to an arc, transforming the contact into a solid-plasma-solid state. However, experiments can only provide a final snapshot of the damage, making it difficult to directly capture the high-speed, transient physical processes occurring at the armature-rail interface during the launch, including current distribution and temperature rise. And these processes are precisely crucial factors driving the changes in contact state and ultimate damage. Therefore, to reveal the intrinsic relationship between damage morphology and dynamic contact states, further simulations of the entire electromagnetic launch process are required.

4 Electrical and Thermal Characteristics of the armature-Rail for Different Contact States

Refer to the phase changes and surface roughness results observed in the experiments, two-dimensional models are constructed for different contact states to analyze the electrical and thermal characteristics at the armature-rail interface.

4.1 Dry sliding contact state

An armature-rail electrical contact model consistent with the geometric dimensions and material parameters of the experimental platform is constructed. The measured pulse current waveform from experiment is applied to one side of the rail, with the other side grounded. To enhance computational efficiency, the armature is treated as stationary and defined as a wall boundary, allowing the air between armature and rail to accelerate backward relative to the armature, forming laminar flow. The air fluid motion can be expressed by the Navier-Stokes equation and the continuity equation

$$\rho\left(\frac{\partial u}{\partial t}+u\cdot\nabla u\right)=-\nabla p+\nabla\cdot\left\{\eta\left[\nabla u+\left(\nabla u\right)^{T}\right]-\frac{2}{3}\eta\left(\nabla\cdot u\right)I\right\}+F \tag{2}$$

$$\frac{\partial\rho}{\partial t}+\nabla\cdot\left(\rho u\right)=0 \tag{3}$$

where, ρ is the fluid density, p is the pressure, η is the fluid dynamic viscosity, and u is the fluid velocity, set as the launch velocity. During dry sliding contact, the behavior within electromagnetic field is governed by Maxwell's equations:

$$\begin{cases} J=\sigma(-\nabla\varphi-\dfrac{\partial A}{\partial t}) \\ E=-\nabla\varphi-\dfrac{\partial A}{\partial t} \\ \nabla\cdot B=0 \\ \nabla\cdot(\sigma\nabla\varphi)+\nabla\cdot(\sigma\dfrac{\partial A}{\partial t})=0 \end{cases} \tag{4}$$

where, J is the normal conduction current density and σ is the material conductivity. φ is the scalar potential of electromagnetic field, A is the vector potential, and t is time. E is the electric field intensity and B the magnetic induction intensity.

In thermal field, the boundary conditions for the rail and air domains with respect to the external environment are set as convective heat flux. Since the model represents half of a two-dimensional axisymmetric system, the interface wall between the armature and the external environment remains its other half, so its boundary condition is set as an inward heat flux. With the air domain treated as fluid heat transfer and the rail and armature as solid heat transfer, their internal heat transfer equations are:

$$\begin{cases} \rho C_p \dfrac{\partial T}{\partial t} + \rho C_p u \cdot \nabla T + \nabla \cdot q = Q \\ q = -k \nabla T \end{cases} \tag{5}$$

where, C_P is the heat capacity of fluid or solid at constant pressure, and k is the thermal conductivity coefficient. Q is the heat production and T the temperature. Under electromagnetic-thermal-fluid coupling, the distribution of current density and temperature of the armature-rail system is shown in Fig. 7.

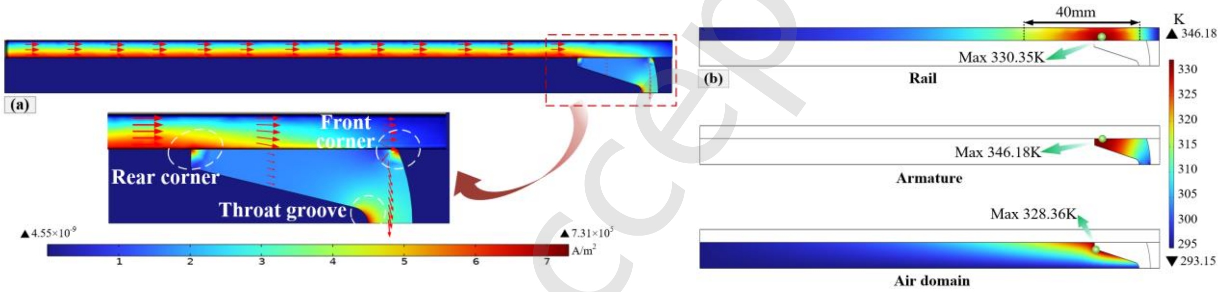

Fig. 7 Electrical and thermal distribution of the armature-rail system under dry sliding contact state: (a) Current density; (b) Temperature.

As depicted in Fig. 7, due to the skin effect, the current density in rail is concentrated within a thickness of approximately 0.5 mm near the inner side. In the armature, it is concentrated in the throat groove and the front and rear corners, reaching up to 7.3×10^5 A/m^2, higher than the 4.6×10^5 A/m^2 in the rail, as regions with higher curvature tend to accumulate more charge. The high-temperature region in the rail is concentrated in a segment approximately 40 mm behind the armature-rail interface, with the highest temperature near the position where it contacts the end of armature tail, reaching 330.35 K. The high-temperature region of the armature is concentrated at the rear end of the tail, decreasing towards the head. Due to natural convection heat transfer between metal and air, the high-temperature region in the air domain is close to the edge in contact with the armature-rail, decreasing outward.

Taking the end of armature as the coordinate origin and the launch direction as the positive direction, the spatiotemporal variation in current density at the armature-rail interface under dry sliding contact state is shown in Fig. 8.

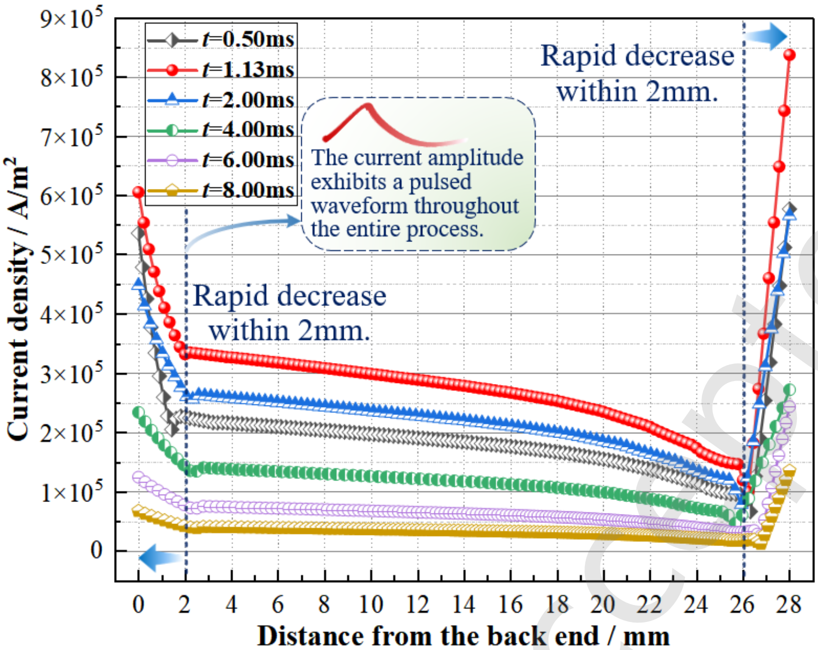

Fig. 8 Variation in current density at the armature-rail interface under dry sliding contact state.

As can be seen from Fig. 8, as the launch progresses, there are two current density extreme points at the armature-rail contact interface with a length of 28 mm. They are located at both ends, consistent with the distribution shown in Fig. 7(a). At the same moment, the current density rapidly decreases within a range of 2 mm from the maximum value at the rear end, then gradually decreases from 2 mm to 26 mm, and finally sharply rises to a higher extreme value within the last 2 mm at the front end.

The variation in temperature at the armature-rail interface is also recorded, as shown in Fig. 9.

As illustrated by Fig. 9, along the launch direction, the temperature exhibits only one extreme value, located within the range of 2.5 mm to 4.7 mm from the contact end. At the same moment, the temperature slowly rises to the peak from the end and then continuously decreases. It is noteworthy that the time when the temperature reaches the peak value of 346.18 K is 2.00 ms, slightly lagging behind the peak current time of 1.13 ms. This is because, when current passes through the conductor, heat is generated due to the Joule effect, but the real-time response of the conductor temperature is not immediately apparent, as the absorption and dissipation of thermal energy is a cumulative process. Therefore, although the current reaches its peak, the temperature peak is constrained by the accumulation and distribution of heat, which also reflects the thermal response characteristics of the armature-rail material. Before 2.00 ms, the position of the highest temperature moves forward continuously as the temperature increases, with the peak points at 0.50 ms, 1.13 ms, and 2.00 ms corresponding to 3.4 mm, 4.0 mm, and 4.7 mm from the end, respectively. After 2.0 ms, the position of the highest temperature gradually moves backward as the temperature decreases. In other words, under the dry sliding contact state, the higher the temperature at the armature-rail contact interface, the closer the highest temperature point is to the armature head, and the wider the high-temperature region at the end.

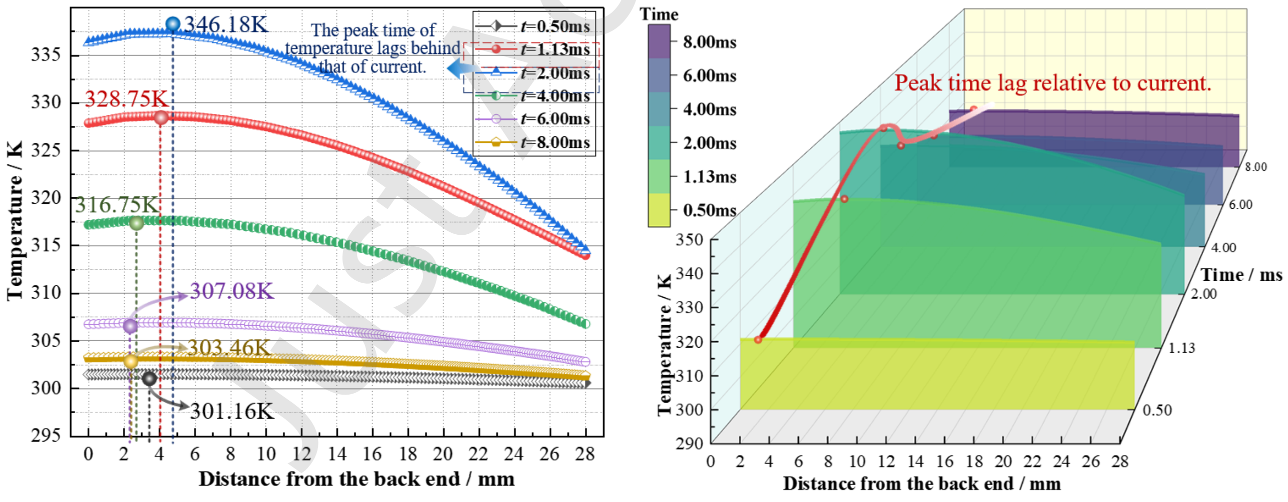

Fig. 9 Variation in temperature at the armature-rail interface under dry sliding contact state.

4.2 Mixed lubrication contact state with dry sliding and LMF coexisting

As the launch proceeds or pulse current peak increases, simulation shows that the armature-rail interface temperature will reach 954.15 K at 130 kA, exceeding the melting point of the 6063-T6 aluminum alloy armature at 888.15-928.15 K. At this point, the dry sliding contact model is no longer applicable, as the solid metal melts and liquefies, forming a LMF at the contact interface. The contact between the armature and rail transitions from solid-solid contact to solid-liquid-solid contact. Meanwhile, from the temperature distribution pattern during dry sliding contact shown in Fig. 9, it can be seen that the high-temperature region extends forward from the armature tail, indicating that the thermal melting of solid metal begins at the rear end. The LMF is set to starting from the rear end, and the schematic of the armature-rail mixed lubrication contact state is shown in Fig. 10.

To characterize the friction coefficient, μ, for different contact states in Fig. 10, the Stribeck lubrication curve is plotted, as shown in Fig. 11.

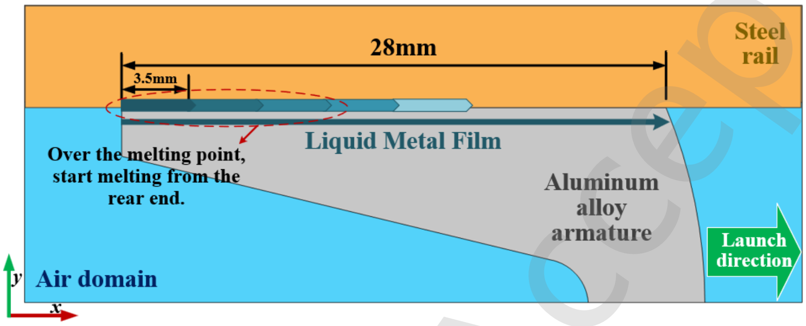

Fig. 10 Schematic diagram of mixed lubrication contact state.

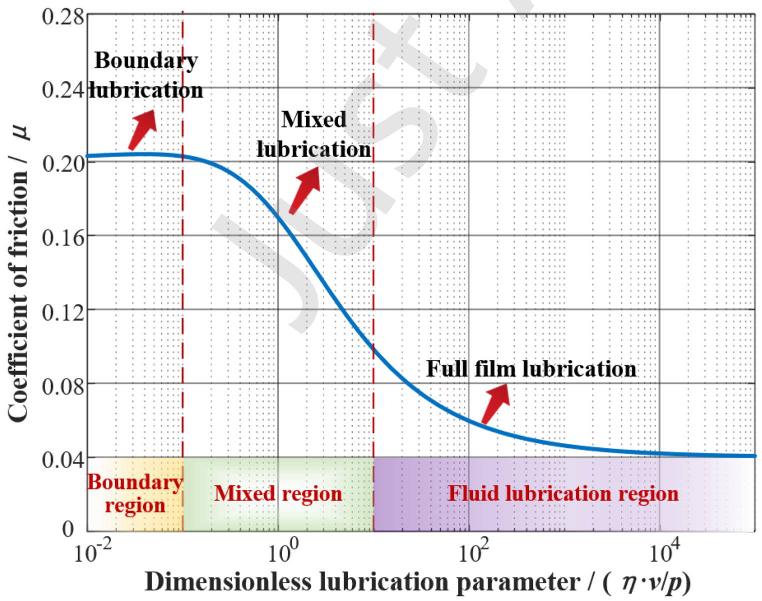

Fig. 11 Stribeck lubrication curve.

The horizontal axis in Fig. 11 is represented by the dimensionless parameter, $\eta \cdot v/p$ to indicate different lubrication states, where η is the lubricant viscosity, v is the velocity, and p is the normal load. At the beginning of launch, v is approximately 0 and p is about 0.61 MPa. With no lubricant present between the armature and rail, the medium at the solid-solid contact interface can be considered rarefied air. Referring to the dynamic viscosity of air at standard temperature and pressure, η is approximated as 3.5×10^{-4}Pa·s [33]. Therefore, when the horizontal coordinate is close to 0, μ is taken as 0.2, corresponding to the boundary lubrication region. As the interface temperature exceeds the liquidus line of aluminum alloy during launch, the formation of LMF between the armature and rail causes the contact state to transition toward the mixed lubrication region. This continues until LMF covers the entire interface, entering the fluid lubrication region. At this stage, v can reach approximately 200 m/s, and p decreases to tens or even a few Pa. Referring to the dynamic viscosity of molten aluminum alloy, η is taken as 1.4×10^{-3}Pa·s [34], and thus μ is set to 0.04.

On the basis of the dry sliding contact model, it is assumed that the thickness of LMF remains constant at 20 μm during launch, undergoing only lateral expansion along the launch direction. Additionally, no slip occurs on the armature surface, and the armature moves forward at the same speed as LMF as a unified whole. Under this assumption, the Reynolds equation, which characterizes the hydrodynamic lubrication behavior of LMF, is further introduced as follows:

$$\nabla \cdot \left(\frac{h^3}{12\eta} \nabla p \right) = \frac{v_r \cdot \nabla h}{2} + \frac{\partial h}{\partial t} \tag{6}$$

here, h represents the LMF thickness, and v_r is the velocity vector of the relative motion at the armature-rail interface. The length of LMF, l_{LMF}, in Fig. 10 is set to 3.5 mm, 7.0 mm, 10.5 mm, 14.0 mm, 17.5 mm, 21.0 mm, 24.5 mm, and 28.0 mm, respectively. Based on the Stribeck lubrication curve in Fig. 11, μ for the areas with and without LMF is set to 0.2 and 0.04, respectively. The variation in current density at the armature-rail interface under the mixed lubrication contact state is shown in Fig. 12.

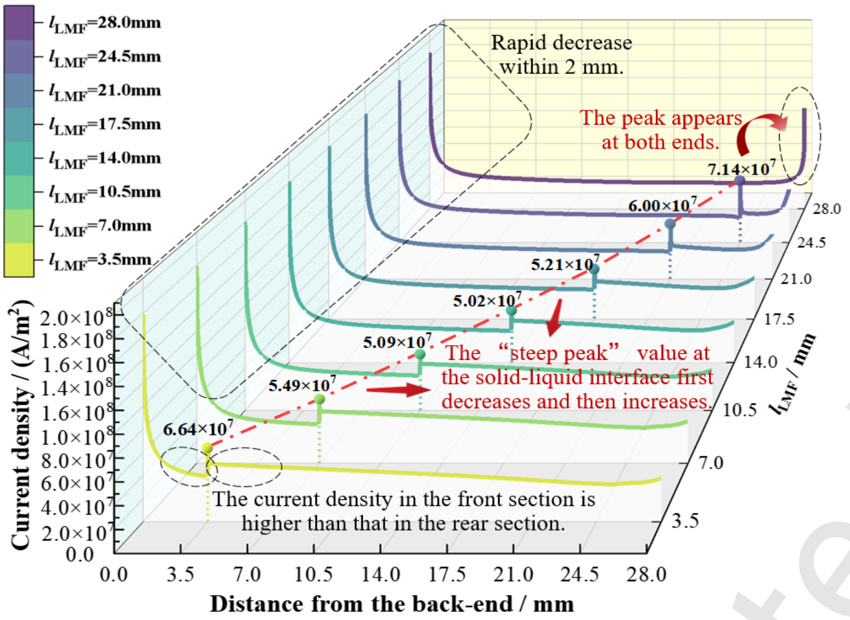

Fig. 12 Variation in current density at armature-rail Interface with l_{LMF}.

From Fig. 12, it can be observed that under the influence of the velocity skin effect, the current density is concentrated at the armature tail, reaching a peak of 1.82×10^8 A/m^2. It rapidly decreases within a 2 mm range before stabilizing, with a slight increase at the front end. When the aluminum alloy melts from solid to liquid, its electrical conductivity decreases from 3.03×10^7 A/m^2 to 3.97×10^6 A/m^2, which causes the current to flow more preferentially into the solid-solid contact region with higher conductivity. Therefore, the current density at the dry sliding contact interface is higher than at the rear end lubrication interface. When the current flows through the solid-liquid interface, due to the sudden change in conductivity and the "optimal path" principle, the current tends to concentrate as much as possible in the solid phase, exhibiting a "steep peak". As l_{LMF} increases, the "steep peak" at the interface first decreases and then increases. When l_{LMF} increases from 3.5 mm to 14.0 mm, the steep peak decreases from 6.64×10^7 A/m^2 to 5.02×10^7 A/m^2. When l_{LMF} increases from 14.0 mm to 24.5 mm, the steep peak rises to 7.14×10^7 A/m^2. This is because, during LMF grows from its initial generation to half the length of armature-rail interface, i.e., 14 mm, the current flowing into LMF continuously increases, leading to a more balanced distribution between the solid and liquid segments, thus reducing the steep peak. However, as the LMF continues to advance and its length exceeds that of the dry sliding contact segment, its impact on the current path strengthens. More current concentrates into the shorter dry sliding contact segment, causing the steep peak to rise. By the time l_{LMF} reaches 28.0 mm, the armature-rail contact transitions to a single solid-liquid-solid contact state. The overall decrease in interface conductivity makes current inflow harder, causing it to concentrate in the tail and head corners with higher curvature, and the peaks of curve appear at both ends.

The variation in temperature at the armature-rail interface is shown in Fig. 13.

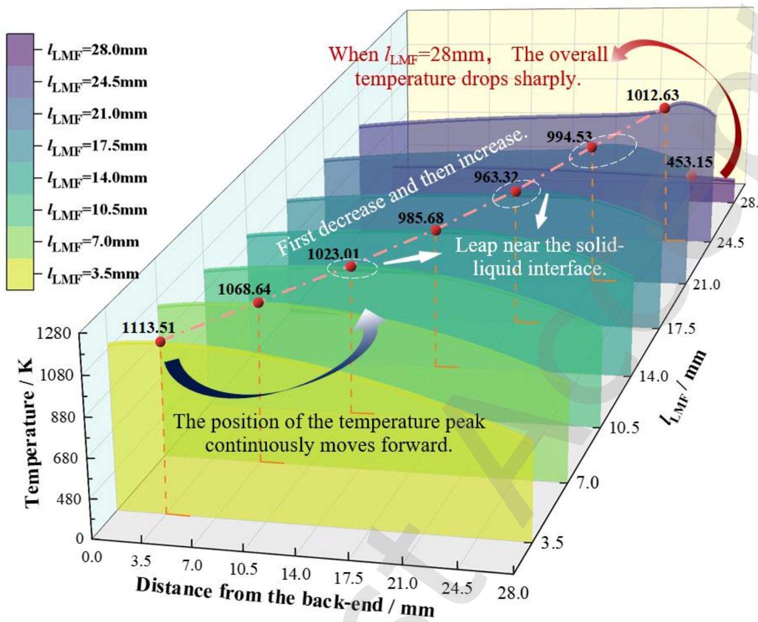

Fig. 13 Variation in temperature at armature-rail Interface with l_{LMF}.

As depicted in Fig. 13, the temperature gradually increases from the rear end, with a noticeable jump near the solid-liquid interface, reaching the peak before continuously decreases. As l_{LMF} increases from 3.5 mm to 24.5 mm, the position of the temperature peak shifts forward. Unlike the case in Fig. 9, which is closer to the tail end, the peak now occurs ahead of the solid-liquid interface, with the highest temperature located in the dry sliding contact region. Regardless of the value of l_{LMF}, the highest temperature is always higher than the 954.15 K observed under dry sliding contact. This is because, when aluminum alloy melts from solid to liquid, its thermal conductivity decreases from 201 W/(m·K) to 90 W/(m·K), weakening its heat conduction capability. Heat accumulates within LMF and is difficult to diffuse, leading to an increase in temperature. Upon entering the dry sliding contact region, the increased thermal conductivity facilitates the diffusion of heat toward the lower-temperature region, causing the temperature at the front-end to continuously decrease. As l_{LMF} increases, the temperature peak at the interface first decreases and then increases. When l_{LMF} increases from 3.5 mm to 17.5 mm, the temperature peak continuously decreases as the overall temperature distribution at armature-rail interface becomes more uniform. As l_{LMF} further increases, the highest temperature point continues to shift forward, exacerbating the melting in dry sliding contact region, which leads to the further expansion of LMF. More heat is concentrated at the front end of the solid-liquid interface and is is less likely to diffuse, causing the temperature peak to rise again. Until l_{LMF} reaches 28.0 mm, the interface temperature drops sharply overall, and the peak decreases from 1012.63 K at l_{LMF} = 24.5 mm to 453.15 K. This is because the armature-rail contact transitions to a single solid-liquid-solid contact state, and the constant pressure heat capacity of liquid Al, 1176.73 J/(kg·K), is much higher than that of solid Al, 900 J/(kg·K). Under the same constant pressure and heat source input, the thermal inertia of LMF increases, leading to a reduced rate of temperature rise at the interface.

4.3 Transition contact state with LMF and plasma gap coexisting

As the launch progresses, on the one hand, during the earlier dry sliding contact phase, the initial contact pressure and high-speed friction cause the micro-protrusions on armature-rail surface to deform, shear, or tear, resulting in a worn rough surface. On the other hand, during the later fluid lubricated contact, the armature continues to accelerate within the rail. Due to velocity lag caused by the inertia of LMF itself or the driving effect of electromagnetic force, some droplets may splash backward. Both the loss of armature material and the splashed droplets adhering to the rail surface create discrete rough protrusions. Simultaneously, the LMF itself shrinks upon cooling or undergoes uneven evaporative contraction, further contributing to contact surface roughness. The gaps generated by these rough interfaces readily trigger loss-contact transition. When transition occurs, the gap is filled with dischargeable gas, and due to the extremely low electrical conductivity of gases, the contact resistance of armature-rail increases sharply. The upper and lower interfaces of the gap form an anode and cathode, creating a high induced electromotive force between the two electrodes, which establishes discharge conditions. The contact state between armature and rail turn to solid-plasma-solid.

Based on spatial frequency and the meta-wave theory, and referring to the measurement results of LSM, a rough contact interface model with gaps is constructed. A completely random distribution of rough curve, $f(x)$, is synthesized using the sum of trigonometric functions expanded by Fourier series

$$\begin{aligned} f(x) &= P\cdot\sum_{\upsilon=-V}^{V} g(\upsilon)\cdot A_{\upsilon}\cdot\cos\left[2\pi\upsilon x+\omega(\upsilon)\right] \\ &= P\cdot\sum_{\upsilon=-V}^{V} a(\upsilon)\left\{\cos(2\pi\upsilon x)\cos\left[\omega(\upsilon)\right]-\sin(2\pi\upsilon x)\sin\left[\omega(\upsilon)\right]\right\} \end{aligned} \tag{7}$$

here, υ represents the spatial frequency of the meta-wave, indicating the number of periodic spatial oscillations per unit distance. A_{υ} is the amplitude, which is multiplied by the Gaussian distribution function, $g(\upsilon)$ to obtain $a(\upsilon)$, and P is the amplitude ratio coefficient. $\omega(\upsilon)$ is the phase angle randomly sampled uniformly in $[-\pi/2, \pi/2]$, and $\pm V$ are the maximum and minimum cutoff values of the spatial frequency.

Furthermore, the upper and lower interfaces of the gap are set as the anode and cathode of the balanced discharge boundary heat source. The magnetohydrodynamic (MHD) modeling of gap arc is performed using the two-fluid equations for electrons and ions, along with Maxwell's equations

$$\nabla\cdot\left(\rho_{\mathrm{i}}\vec{v}^{2}\right)=c_{\mathrm{i}}en_{\mathrm{i}}\vec{E}+c_{\mathrm{i}}n_{\mathrm{i}}\vec{R}_{\mathrm{ie}}+c_{\mathrm{i}}n_{\mathrm{i}}\vec{R}_{\mathrm{ie}}^{T}+c_{\mathrm{i}}en_{\mathrm{i}}\left(\vec{v}\times\vec{B}\right)-\nabla P_{\mathrm{i}} \tag{8}$$

here, ρ_i, n_i, and c_i represent the ion density, ion number, and average ion charge, respectively. v is the ion migration velocity, and P_i is the ion pressure. e is the electron charge. R_{ie} is the momentum exchange term between electrons and ions. The gap formation starts from the rear end still, and the armature-rail transition contact state is shown in Fig. 14.

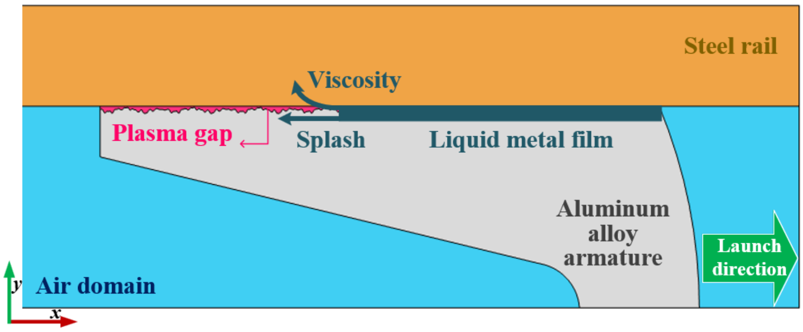

Fig. 14 Schematic diagram of transition contact state.

The gap length l_{plm} in Fig. 14 is set to 4 mm, 8 mm, 12 mm, 16 mm, 20 mm, and 24 mm, respectively. Taking l_{plm} = 20 mm as an example, the temperature, current density, and discharge energy flux density distributions at the armature-rail interface are shown in Fig. 15.

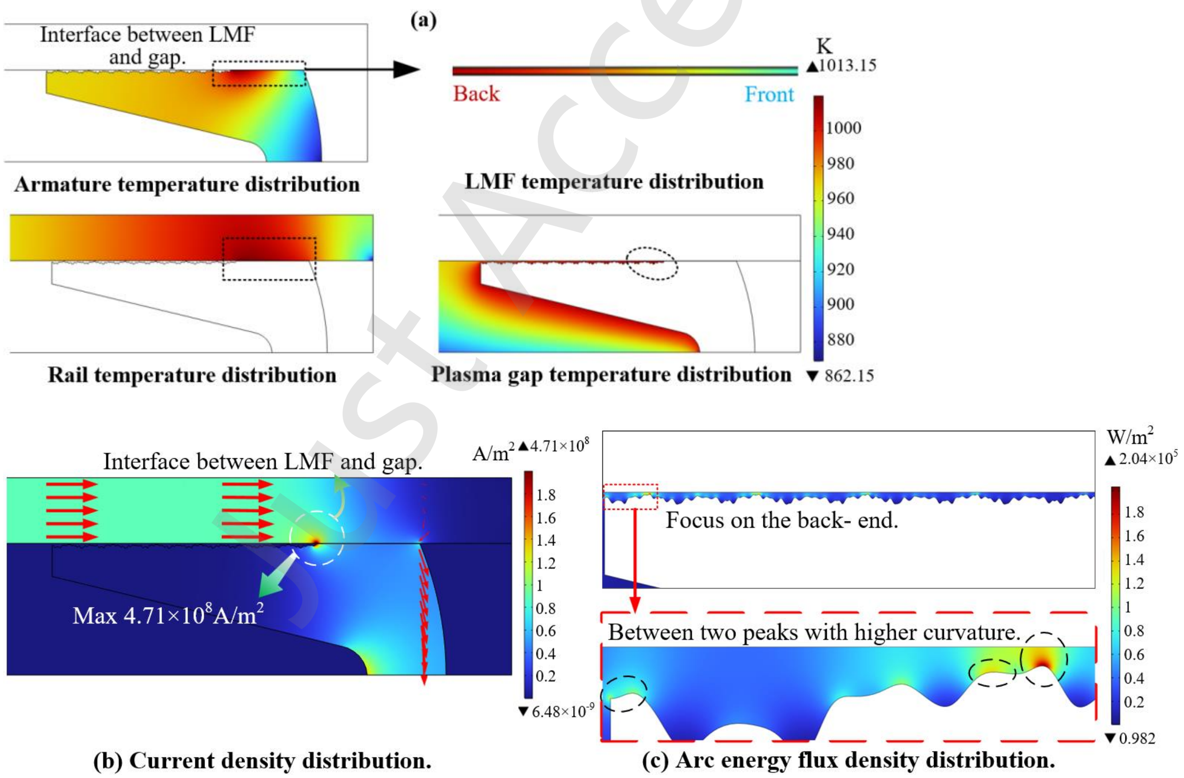

Fig. 15 Distribution of armature-rail interface temperature, current density, and discharge energy flux density.

As can be seen in Fig. 15, the high-temperature regions of the armature, rail, and plasma gap are concentrated at the interface between LMF and gap, decreasing towards the surroundings, with a faster decline at the front end. The high resistivity of air gap makes it difficult for current to flow, causing it to prefer entering the armature from the rear end of LMF. The peak current density is also located at the interface between LMF and gap. The discharge energy flux density is concentrated at the rear end, especially between the two peaks with higher curvature in the rough interface.

The variation in current density at the armature-rail interface for different l_{plm} is shown in Fig. 16.

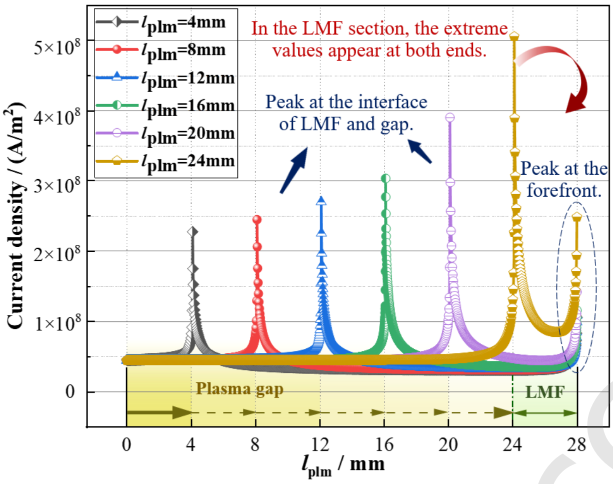

Fig. 16 Variation in current density at armature-rail interface with l_{plm}.

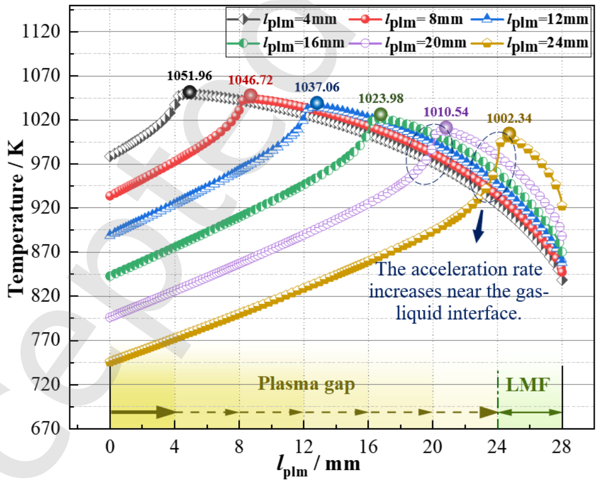

Fig. 17 Variation in temperature at armature-rail interface with l_{plm}.

As indicated in Fig. 16, the current density exhibits two peaks, located at the interface between LMF and gap, and at the front end, with the first peak being higher. It remains relatively stable elsewhere, averaging approximately 4.5×10^7 A/m^2. This indicates that the current is concentrated at the gas-liquid interface. Once the induced electromotive force in the gap reaches discharge level, this current provides the necessary charge for sustained arcing. In the LMF region, the distribution pattern of current density is consistent with the case when l_{LMF} = 28 mm in Fig. 12, where the peaks appear at both ends. As l_{plm} increases, the position of the maximum current density shifts forward, and the value continuously increases. This is due to material loss caused by factors such as LMF splashing and adhesion, resulting in an increasingly longer discharge gap. Consequently, more current is forced to converged in the increasingly shortened, high-conductivity LMF region.

The variation in temperature at the armature-rail interface with l_{plm} is shown in Fig. 17.

As illustrated by Fig. 17, the temperature first increases and then decreases. In the gap region, the temperature continuously rises along the launch direction, accelerating near the gas-liquid interface, reaching a peak just ahead of the interface, and then gradually decreasing in the LMF region, consistent with the distribution in Fig. 15(a). This is because, in the transition contact state, the primary heat source at armature-rail interface comes from the viscous frictional heat generated by LMF. Due to the velocity and current skin effect, the highest temperature is located at the end of LMF, decaying towards both ends. In the discharge gap, although the overall temperature is lower than at the front end of LMF, as seen in Fig. 15(c), the arc, as a high-energy discharge phenomenon, concentrates energy locally at the metal spikes, forming extremely high magnitude of energy flux density. This impacts the contact surface, making it more rough and uneven due to melting and peeling. Additionally, the electromagnetic force impact and the oxidation effect on the metal induced by arc will alter the microscopic structure of the contact surface, severely degrading the contact state. The closer to the gas-liquid interface, the faster the temperature rise, because of the sudden change in conductivity and the "optimal path" principle, where the current converges at the interface, resulting in higher thermal power and temperature. As l_{plm} increases, the overall interface temperature decreases, with the peak dropping from 1051.96 K to 1002.34 K. This is because, on one hand, the concentration of local heat weakens, and thermal diffusion strengthens, while on the other hand, the LMF shortens, thereby reducing viscous frictional heat.

5 Discussion

During electromagnetic launch process, the armature-rail interface is subjected to the combined effects of frictional force and heat. The frictional force is determined by the contact pressure and the coefficient of friction, while the contact pressure is mainly provided by the normal component of the Lorentz force. The primary sources of heat include Joule heat and frictional heat. The complex thermal and mechanical interactions cause frictional wear, directly affecting the contact quality of armature-rail interface. Considering dry sliding, mixed lubrication, and transition contact states, the maximum current density, highest temperature, and their positions at the armature-rail interface are shown in Fig. 18.

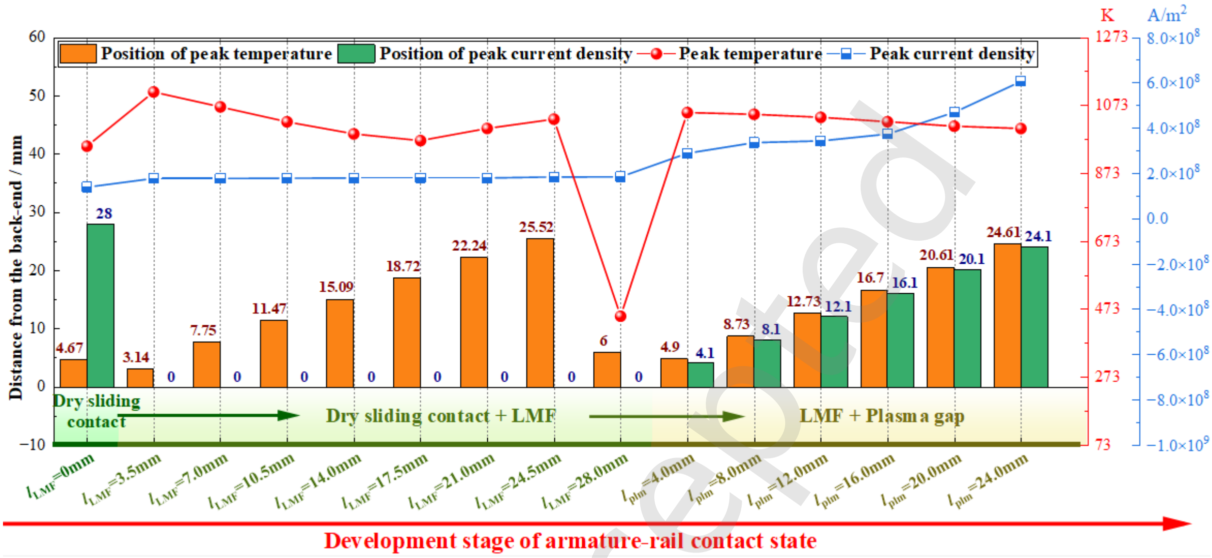

Fig. 18 Maximum current density, highest temperature, and their positions under different contact states.

As depicted in Fig. 18, in the dry sliding contact state, the peak current density is located at the very front of the interface, while the temperature peak is at the tail end, 4.67 mm away. When entering the mixed lubrication contact state with LMF, the peak current density shifts to the tail end. As LMF lengthens, the position of peak temperature continuously moves forward, always about 1 mm ahead of the solid-liquid interface. This provides a sustained high-temperature environment for melting at the front end of the armature, causing LMF to extend further. When LMF reaches 28 mm, the armature-rail interface transitions to a fully fluid-lubricated state, and the temperature peak abruptly drops from 1012.63 K to 453.15 K, with its position returning to 6 mm from the rear end. In the final transition contact stage, due to the high-energy arc heating, the temperature peak rises again to 1051.96 K, and the current density peak increases as well. As l_{plm} grows, the positions of both continuously move forward, further driving the extension of the gap. In other words, the armature-rail interface enters a sustained degradation feedback loop.

To quantitatively assess the evolution of the metal phase and contact state, the rail current and muzzle voltage during launch were measured, as shown in Fig. 19.

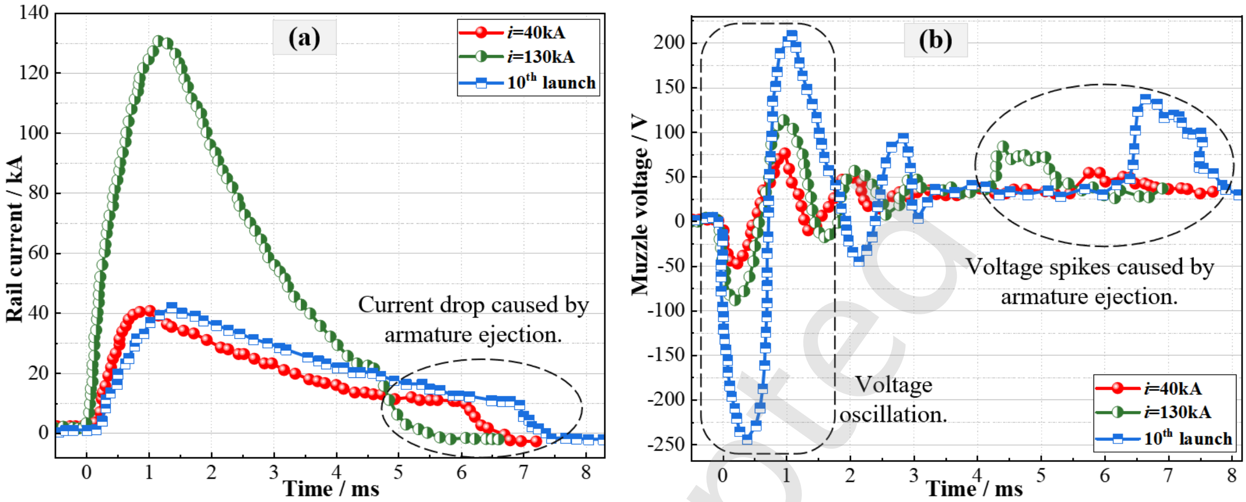

Fig. 19 Rail current and muzzle voltage. (a) Rail current. (b) Muzzle voltage.

In Fig. 19, the rail current exhibits a pulsed waveform, with a sudden drop at the moment of armature exiting the muzzle due to the disconnection of mechanical contact. Owing to the presence of capacitive and inductive components in the circuit, the muzzle voltage displays oscillatory characteristics in the initial phase before stabilizing at a lower level. Ultimately, a spike appears when the armature exits. The contact resistance, R_c, between the armature and rail is calculated based on the muzzle voltage, U, and rail current, I, with U being expressed as:

$$U = IR_r + IR_a + IR_c \quad (9)$$

where, R_r is the volume resistance of rail and R_a of armature, which can be expressed as:

$$\begin{cases} R_r = R_{r0} + \dfrac{1}{h_r}\sqrt{\dfrac{32\mu_{mr}\rho_r}{9\pi t}} \\ R_a = \dfrac{d_r}{h_r}\sqrt{\dfrac{\mu_{ma}\rho_a}{2\pi t}} \end{cases} \quad (10)$$

where, R_{r0} is the initial static resistance, h_r is the height of rail, and d_r is the distance between two rails. μ_{mr} and μ_{ma} are the magnetic permeabilities of the rail and armature, respectively, while ρ_r and

ρ_a are their electrical resistivities. Substituting (10) into (9), the contact resistance, R_c is obtained as

$$R_c = \frac{U}{I} - R_{r0} - \frac{1}{h}\sqrt{\frac{32\mu_{mr}\rho_r}{9\pi t}} - \frac{d}{h}\sqrt{\frac{\mu_{ma}\rho_a}{2\pi t}} \tag{11}$$

Substituting the measured voltage and current data into (11), where the absolute values of U and I are taken to prevent negative resistance values. The contact resistance variation obtained via MATLAB is shown in Fig. 20, along with the evolution of armature-rail contact state illustrated schematically in Fig. 21.

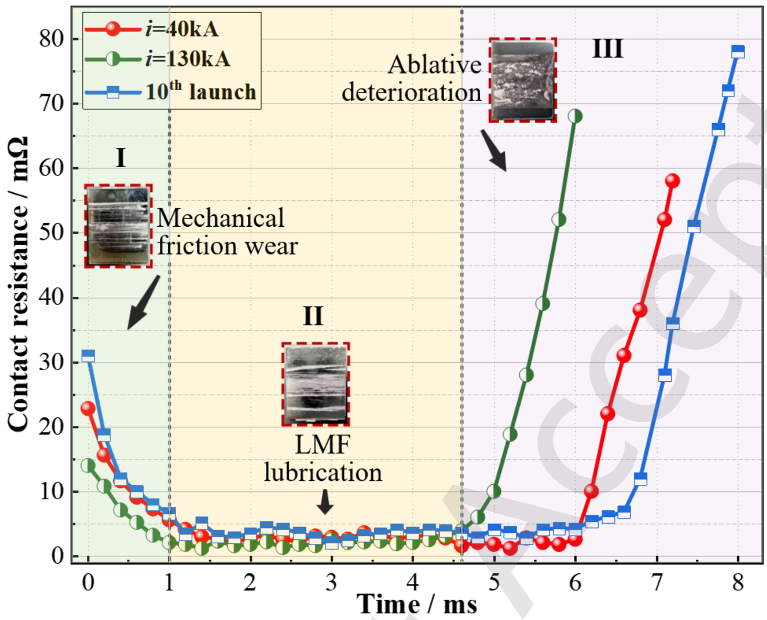

Fig. 20 Variation in contact resistance.

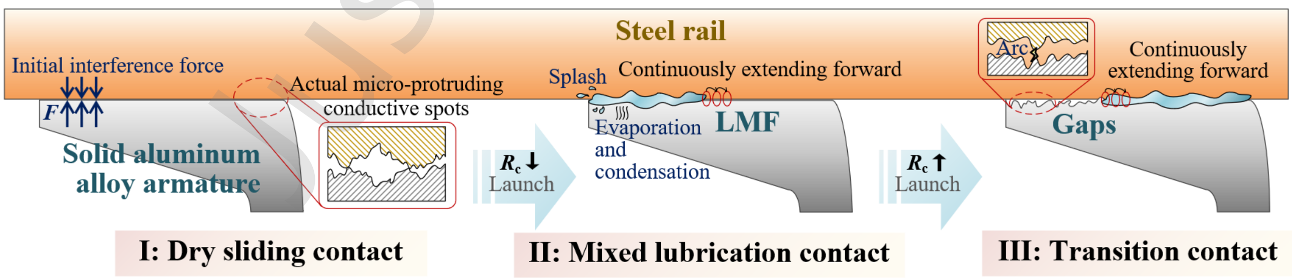

Fig. 21 Schematic diagram of armature-rail contact state evolution.

As presented in Fig. 20, the contact resistance can also be roughly divided into three stages. The first stage occurs during the rising edge of the pulse current, where the contact resistance exhibits an initial peak followed by a gradual decrease. According to Holm's microscopic contact resistance theory, the actual contact between the armature and rail is formed by countless micro-protruding conductive spots on the surface, as illustrated in stage I of Fig. 21. During the early phase of launch, the pulse current is relatively low, and the electromagnetic force has not yet fully developed, thereby the contact pressure is primarily provided by the initial loading interference force. At this point, mechanical friction wear primarily occurs between the armature and rail, as demonstrated in Fig. 2, where the position I on the rail shows scratches or grooves caused by scraping. As the current increases, the velocity and temperature rise, and the accumulation of heat causes the aluminum alloy armature to continuously melt. The armature-rail interface transitions to a solid-liquid-solid contact state, and the increase in contact area reduces the contact resistance. This decrease in contact resistance results in reduced Joule heat, which in turn leads to a downward trend in temperature, as curves shown in Fig. 18. The contact area decreases again, and the heat accumulates until a stable LMF eventually forms. In the second stage, the contact resistance stabilizes at a small value close to zero. The presence of LMF has a positive effect on armature-rail contact. On one hand, it fills the microscopic rough interface, transforming dry friction into internal liquid film friction, thereby reducing the friction coefficient and frictional heat, exerting a "lubrication effect". On the other hand, it increases the conductive contact area and itself has high electrical conductivity, which lowers Joule heat, exerting a "current-collecting effect". At this point, the armature-rail contact is good, as shown in Fig. 2, where wear at R1-3 and R2-3 is minor, with slight deposition marks. However, it should also be noted that due to motion inertia, speed differences, or cooling, the splashing or deposition of LMF may cause material loss, leading to the formation of gap arcs between armature and rail. As the current increases or the number of launch increases, the rupture and instability of LMF becomes a key factor in triggering the transition of electrical contact [35]. R2-3 and R3-3 in Fig. 2 exhibit worsened damage due to friction and ablation. In the third stage, the contact resistance surges abruptly when mechanical and conductive contacts disconnect simultaneously as the armature exits the muzzle. At this point, minute gap arcs at the interface may escalate into severe muzzle arcing. This phenomenon not only occupies the current circuit with high-resistance plasma, but also causes severe erosion and damage to the rail, as shown at position IV in Fig. 2. In the development of electromagnetic launch equipment, muzzle protection design is particularly important.

Based on the above research findings, in practical engineering applications, the front-end of rail should prioritize the optimization of wear resistance and reduce surface roughness. Effective cooling and lubrication techniques are also promising, as they can reduce the splashing and deposition of LMF, maintain the close fit of armature-rail, and improve electrical contact performance. In the muzzle segment, it is recommended to install arc suppression devices or insulating coatings to inhibit the generation of arcs, and to reasonably design shock absorption or damping systems to resist the high-temperature and high-pressure impacts caused by arcs. Additionally, selecting appropriate high-strength alloys and heat- and corrosion-resistant materials can help extend the service life of the device. Moreover, the constructed simulation models can compensate for the limitations of experimental conditions and costs, enabling predictions of electrical and thermal changes in armature-rail at different operating conditions, thereby providing a basis for the selection of metallic materials and the design of cooling systems.

6 Conclusions

In order to investigate the rail damage and contact state evolution characteristics during the electromagnetic launch process, guiding the optimization design of the device, this paper conducted launch experiments with SEM, EDS, and LSM tests. Combined with thermal-electrical characteristic simulation and contact resistance analysis, the evolution characteristics of the armature-rail contact state were revealed. The following statements hold for the provided work:

1) The front segment of rail mainly experiences mechanical friction, while in the middle, LMF is generated due to the melting of aluminum alloy armature, reducing the wear roughness. At the rear segment, severe damage occurs due to arc ablation. Increasing pulse current peak or the number of

launch intensifies wear.

2) In dry sliding contact state, the current density in armature-rail is concentrated in regions with high curvature. The temperature at the rear end is higher, and the peak point moves forward with temperature rise, promoting the formation of LMF. In mixed lubrication contact, current density and high-temperature regions are concentrated at the rear, with abrupt changes at the solid-liquid interface. In transition contact state, current density and temperature reach their extreme values at the gas-liquid interface, leading to irreversible degradation of contact quality.

3) The contact resistance between armature and rail can be divided into three stages. Initially, it is large due to mechanical wear. Then, it decreases steadily with the generation and lubrication of LMF, and finally, it sharply increases due to the appearance of arc plasma. Therefore, the front segment of rail should enhance wear resistance, the middle segment should optimize lubrication, and the muzzle requires comprehensive protection against heat, wear, and impact.

Acknowledgements

This work was supported in part by the National Natural Science Foundation of China Grant 92266112 and Beijing Natural Science Foundation Grant 3242024.

Declaration of competing interest

The authors have no competing interests to declare that are relevant to the content of this article.

References

[1] Yu K X, Zhu H T, Xie X F, Duan H J, Ding J M, Sun C P. Loss analysis of air-core pulsed alternator driving an ideal electromagnetic railgun. *IEEE Trans Transp Electrif* **7**(3): 1589-1599 (2021)

[2] Liao G W, Wang W, Wei C J, Zhao H, Liu X J. Characterization of magneto-thermo-

hydrodynamic lubrication of metal liquid film at armature/rail interface. *Tribology Int* **189**: 108912 (2023)

[3] Cai Z B, Li C L, You L, Chen X D, He L P, Cao Z Q, Zhang Z N. Prediction of contact resistance of electrical contact wear using different machine learning algorithms. *Friction* **12**: 1250-1271 (2024)

[4] Yan R G, Wang X Q, Zhao H K, Zhao W Y. Research on the motion and temperature characteristics of electromagnetic energy propulsion devices considering dynamic contact resistance. *High Volt Eng* **50**(10): 4749-4759 (2024)

[5] Zhou Y, Cao R G, Li P, Ma X, Hu X Y, Li F D. A damage detection system for inner bore of electromagnetic railgun launcher based on deep learning and computer vision. *Exp Syst Appl* **202**: 117351 (2022)

[6] Ren S D, Feng G, Liu S W. Study on wear of electromagnetic railgun. *IEEE Access* **10**: 100955-100963 (2022)

[7] Chen L X, He J J, Xiao Z, Xia S G, Feng D, Tang L L. Experimental study of armature melt wear in solid armature railgun. *IEEE Trans Plasma Sci* **43**(5): 1142-1146 (2015)

[8] Li B, Lu J Y, Tan S, Zhang Y S, Cai X Y. Study on dynamic wear process of high-speed sliding electric contact armature surface. *Trans China Electrotechnical Soc* **38**(1): 131-139 (2023)

[9] Li C X, Dong Z Y, Shen S F, Liu L M, Hou J X, Xu J H. Influence of armature/rail structure coordination on the evolution of rail deposition layer. *IEEE Trans Plasma Sci* **52**(8): 3294-3302 (2024)

[10] Du P P, Lu J Y, Li X P, Feng J H, Li K. Interior ballistic characteristics of electromagnetic rail launcher considering the dynamic characteristics of real launcher. *IEEE Trans Ind Electron* **68**(7): 6087-6096 (2021)

[11] Gao X, Liu F, Feng Y, Zhang H H, Zhan Z J. Wear characteristics of rail-armature under the action of interference fit and Lorentz force. *IEEE Trans Plasma Sci* **48**(6): 2261-2265 (2020)

[12] Guo A X, Du X Y, Wang X Z, Liu S W. Calculation of armature melting wear rate based on

contact surface heat distribution. *IEEE Trans Plasma Sci* **52**(7): 2981-2990 (2024)

[13] Li B, Lu J Y, Tan S, Jiang Y Z, Zhang Y S. The influence of roughness of sliding electrical contact interface on the melting characteristics of armature. *Trans China Electrotechnical Soc* **33**(7): 1607-1615 (2018)

[14] Cheng W, Yuan W, Zhao Y, Yan P. Effects of armature characteristics on armature-rail contact performance. *IEEE Trans Plasma Sc* **45**(7): 1380-1386 (2017)

[15] Ge X, Cao B, Wang Z, Pei P C, Huang K, Chen Y H. Research on the contact characteristics between armature and rail of the enhanced electromagnetic rail gun based on the new aluminum alloy armature. *IEEE Trans Plasma Sci* **51**(12): 3703-3708 (2023)

[16] Ma S, Lu S L, Ma H T, Wang H, Nong A B, Ma D D. Investigation on the spatial-temporal distribution of electromagnetic gun rail temperature in single and continuous launch modes. *IEEE Trans Plasma Sci* **50**(7): 2270-2278 (2022)

[17] Yang C F, Ren Q, Dai F, Cheng J S, Xiong L, Li P Y. A new electro-thermal simulation approach for moving electromagnetic rail launchers. *IEEE J Multiscale Multiphys Comput Tech* **9**: 279-289 (2024)

[18] Yao J M, Xia S G, Chen L X, He J J. Analysis of the melt erosion patterns at rail-armature contact of rail launcher in current range of 10-20 kA/mm. *IEEE Trans Plasma Sci* **47**(3): 1674-1680 (2019)

[19] Li B, Ma W M, Lu J Y, Tan S, Zhang Y S, Cai X Y. Effects of supply current and armature structure on melting characteristics of armature surface in sliding electric contact. *IEEE Trans Plasma Sci* **47**(1): 721-728 (2019)

[20] Ruan J H, Chen L X, Xiong Y, Li C X, Xia S G. A 3-D magneto-elastohydrodynamic model of liquid metal film at rail-armature interface. *IEEE Trans Plasma Sci* **48**(7): 2628-2634 (2020)

[21] Wang Z J, Chen L X, Cheng W P, Yuan W Q, Xu W D, Yan P. Influence of magnitude of armature interference on static contact resistance. *IEEE Trans Plasma Sci* **52**(4): 1507-1514 (2024)

[22] Li S, Wang X, Zhang S, Jin L, Liu P. Study on the lumped evaluation model of sliding electrical contact performance of railgun. *IEEE Trans Plasma Sci* **47**(5): 2404-2411 (2019)

[23] Liu S, Du X, Guan J, Shi J. Research on transient contact characteristics of the hyperbolic rail augmented quadrupole launcher. *IEEE Trans Plasma Sci* **50**(10): 3794-3801 (2022)

[24] Wu Y H, Xu J, Zhu J J, Xu W. Research on electrical contact characteristics of brush-rail device with transient large current. *IEEE Access* **11**: 37560-37569 (2023)

[25] Yan R G, Zhao H K. Multi-physical field coupling dynamic numerical modeling for augmented rail launchers. *IEEE Trans Magn* **61**(3): 1-4 (2025)

[26] Du W T, Cheng L, Long X L, Lu J Y, Li S C. Research on equivalent test method for electromagnetic track launch magnetic field environment. *J Ordnance Equip Eng* **43**(5): 138-145 (2022)

[27] GB/T 699-2015. Quality carbon structure steels. Beijing: *Standards Press of China* (2015)

[28] GB/T 6892-2023. Wrought aluminium and aluminium alloys extruded profiles for general engineering. Beijing: *Standards Press of China* (2015)

[29] Xia S G, Hu Y Y, Chen L X, He J J, Yuan Z, He H X. Experimental studies on melt erosion at rail-armature contact of rail launcher in current range of 10-20 kA/mm. *IEEE Trans Plasma Sci* **45**(7): 1667-1672 (2017)

[30] Zhang J W, Lu J Y, Tan S, Li B, Zhang Y S. Research status of surface damage of electromagnetic rail launch equipment. *Acta Armamentarii* **44**(7): 1908-1919 (2023)

[31] Watt T, Motes D T. The effects of surface coatings on the onset of rail gouging. *IEEE Trans Plasma Sci* **39**(1): 168-173 (2011)

[32] Gao Y, Wang Z X, Xiao H C, Xu Y T, Li B M. Numerical analysis of arc motion at the muzzle of electromagnetic railgun under reflux effect. *Mech Pract* 42(3): 331-336 (2020)

[33] Ma G, Li C, Zhu Z P, Liu Z Y, Huang J W, Zhang A Y. The dynamic viscosity of air is measured by Hall element based on pendulum experiment. *Phys Exp Coll* **35**(2): 45-48 (2022)

[34] Li C S, Liu H O, He W, Hao Z G, Zhao T, Zhang L. Viscosity and effect factors of aluminium alloy melt. *Light Alloy Fab Technol* (10): 22-25 (2005)

[35] Ruan J H, Chen L X, Wang Z J, Li C G, Wu P F, Xia S G. Transition mechanism based on load imbalance of liquid metal film. *IEEE Trans Plasma Sci* **48**(10): 3720-3726 (2020)

Luyao LIU received the B.Sc. degree in electrical engineering from Shandong University, Shandong, China, in 2022. She is currently pursuing the Ph.D. degree at Shandong University. Her research interests focus on the analysis of armature-rail electrical contact performance and combustion arc ablation.

Hongshun LIU (Member, IEEE) received the B.Sc. and Ph.D. degrees in electrical engineering from Shandong University, Shandong, China, in 2004 and 2010, respectively. He is currently an Associate Professor of Electrical Engineering at Shandong University. His research interests include the modeling and simulation for power system electromagnetic transient processes, overvoltage and insulation coordination, and partial discharge theory and its applications.